
ConDiff: A Challenging Dataset for Neural Solvers of Partial Differential Equations

Vladislav Trifonov

Skoltech

vladislav.trifonov@skoltech.ru

Alexander Rudikov

AIRI

Skoltech

Oleg Iliev

Fraunhofer ITWM

Ivan Oseledets

AIRI

Skoltech

Ekaterina Muravleva

Skoltech

Abstract

We present ConDiff, a novel dataset for scientific machine learning. ConDiff focuses on the diffusion equation with varying coefficients, a fundamental problem in many applications of parametric partial differential equations (PDEs). The main novelty of the proposed dataset is that we consider discontinuous coefficients with high contrast. These coefficient functions are sampled from a selected set of distributions. This class of problems is not only of great academic interest, but is also the basis for describing various environmental and industrial problems. In this way, ConDiff shortens the gap with real-world problems while remaining fully synthetic and easy to use. ConDiff consists of a diverse set of diffusion equations with coefficients covering a wide range of contrast levels and heterogeneity with a measurable complexity metric for clearer comparison between different coefficient functions. We baseline ConDiff on standard deep learning models in the field of scientific machine learning. By providing a large number of problem instances, each with its own coefficient function and right-hand side, we hope to encourage the development of novel physics-based deep learning approaches, such as neural operators and physics-informed neural networks, ultimately driving progress towards more accurate and efficient solutions of complex PDE problems.

1 Introduction

In recent years, machine learning techniques have emerged as a promising approach to solving PDEs, offering a new perspective in scientific computing. Machine learning algorithms, especially those based on neural networks, have demonstrated success in approximating complex functions and physical phenomena. Neural networks can provide more efficient and scalable methods compared to traditional numerical methods, which can be computationally expensive and limited by the dimensionality of the problem to be solved. Approaches using physical losses Karniadakis et al. [2021], operator learning Li et al. [2020], symmetries incorporation Wang et al. [2020], data-driven discretization Bar-Sinai et al. [2019] lead to more physically meaningful solutions and gave neural networks better recognition than just black-boxes.

Classical methods for solving PDEs have been extensively developed and refined over the years, providing a basis for understanding and analyzing various physical phenomena. These methods involve discretization the PDEs using techniques as the finite difference method LeVeque [2007], finite element method Bathe [2006], finite volume method Eymard et al. [2000] or spectral methods Trefethen [2000], followed by numerical solution of the resulting algebraic equations. While these methods have been successful in solving a wide range of PDEs, they often face the curse of

dimensionality when parametric PDEs need to be solved in connection with optimization, optimal control, parameter identification, uncertainty quantification. The reduction of complexity for such classes of problems can be addressed with surrogate models using machine learning.

The main approaches in scientific machine learning are (i) using governing equations as loss functions with physics-informed neural networks Karniadakis et al. [2021], Cai et al. [2021], Eivazi et al. [2024], Raissi et al. [2019]; (ii) learning mappings between infinite-dimensional function spaces with neural operators Li et al. [2020], Fanaskov and Oseledets [2023], Lu et al. [2021a], Li et al. [2024], Tran et al. [2021]; (iii) hybrid approaches where machine learning techniques are incorporated into classical simulations Brunton and Kutz [2022], Schnell and Thuerey [2024], Hsieh et al. [2019], Ingraham et al. [2018].

These surrogate models have shown significant potential in solving parametric PDEs, but a critical aspect of their development remains the availability of comprehensive datasets for validation. The accuracy and reliability of these machine learning-based approaches are highly dependent on the quality and diversity of the data used to train and test them. Without such datasets, the performance and generalization ability of these models cannot be adequately assessed, and their applicability to real-world problems may be limited. As new techniques and methods emerge in the future, the need for robust and extensive datasets will only increase. It is therefore essential to develop approaches to the curation of high quality datasets that can support the development and validation of innovative approaches to solving complex problems in different scientific and engineering domains.

With ConDiff (short for Contrast Diffusion), we propose a novel dataset that complements existing datasets and provides an approach to generating complex coefficients for parametric PDEs that can address real-world problems. We also provide a measurable metric for the complexity of the dataset and validate our approach on a list of well-known models.

The ConDiff dataset is available on the Hugging Face Hub: <https://huggingface.co/datasets/condiff/ConDiff>. The code with ConDiff generation, usage, validation and requirements is available at: <https://github.com/condiff-dataset/ConDiff>.

2 ConDiff

Motivation Creating a comprehensive benchmark for classes of parametric PDEs is a particular challenge for the scientific machine learning community. The main challenges in creating a comprehensive dataset are: (i) computational complexity; (ii) storage complexity for the desired dimensions of the discretized PDE and parameter space; (iii) properties of the coefficients and solution functions; (iv) relation to real-world problems. The first and second reasons illustrate a technical bottleneck in the creation of the dataset and are mostly dependent on the hardware and efficiency of the numerical method used. Properties such as coefficient smoothness, discontinuity, spatial variation of the coefficients, variance of the parametric space significantly affect the complexity of the dataset and should be carefully chosen. The solution to PDEs (i.e. the ground truth for the dataset) depends on a number of numerical aspects such as choice of mesh, discretization, numerical algorithm, boundary and initial conditions. Therefore, it is very important to consider every little detail regarding different numerical schemes, PDEs, boundary and initial conditions.

Existing benchmarks and datasets cover different aspects of scientific machine learning for different classes of PDEs and can be divided into several groups. PDEBench Takamoto et al. [2022], PIN-Nacle Hao et al. [2023], CFDBench Luo et al. [2023] have a large number of PDEs with different boundary and initial conditions and different dimensionality and resolution. The best covered area is weather forecasting: SuperBench Ren et al. [2023], ClimSim Yu et al. [2024], DynaBench Dulny et al. [2023], OceanBench Johnson et al. [2024], ChaosBench Nathaniel et al. [2024]. There are also domain specific datasets with applications to Lagrangian mechanics LagrangeBench Toshev et al. [2024] and phase change phenomena BubbleML Hassan et al. [2023]. Worth noting frameworks for differential simulations and general environments for PDEs in scientific machine learning: PDE Control Gym Bhan et al. [2024], PDEArena Gupta and Brandstetter [2022], DiffTaichi Hu et al. [2019], DeepXDE Lu et al. [2021b] and Φ_{Flow} Holl et al. [2020].

While all of these datasets contribute significantly to the community, to the best of the authors' knowledge there is no dataset dedicated to the very important class of academic and real-world problems, the class of parametric PDEs with random coefficients. Typically, when a new model is

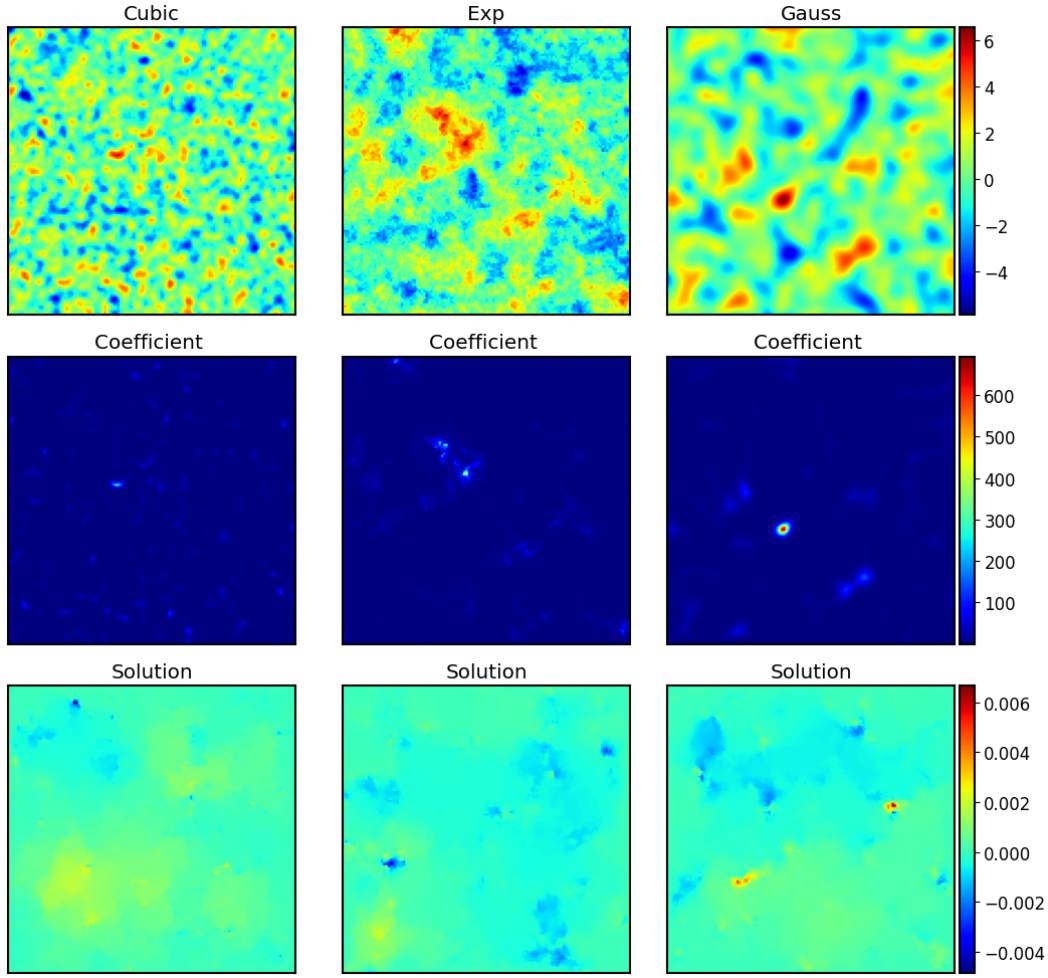


Figure 1: Visualization of the GRF (top row), the coefficient $k(x)$ generated from this GRF (middle row) and the corresponding solution of the equation (1) (bottom row) for a sampled PDEs with grid 128×128 and $\sigma^2 = 2.0$.

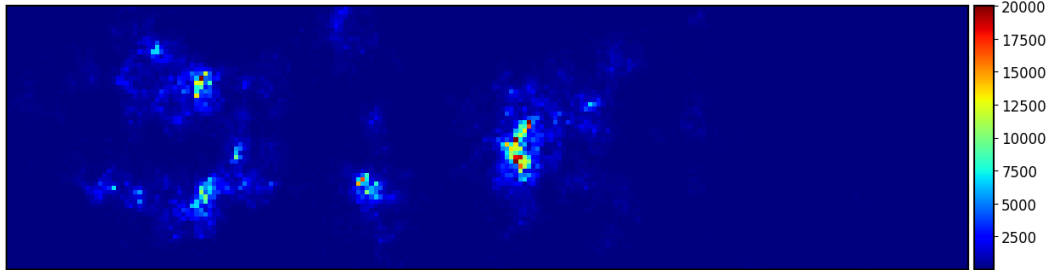


Figure 2: Cross section of the x -permeability field along the z axis over the SPE10 model 2 with $z = 4$.

proposed, authors test it with a set of equations with smooth coefficients Brandstetter et al. [2022], Nguyen et al. [2023], Ripken et al. [2023], Bryutkin et al. [2024]. Such coefficients do not allow important classes of industrial applications to be addressed. In section 3 we show that increasing

the heterogeneity and contrast in the coefficient function leads to increasing challenges in building accurate surrogate models.

Problem definition Existing benchmarks Takamoto et al. [2022], Hao et al. [2023], Luo et al. [2023] cover a set of PDEs, both steady-state and time-dependent, with different resolutions and time lengths. In our work, we approach the problem from the other side tackling a fixed parametric PDE and generating a comprehensive set of random coefficients for it. We consider a 2D steady-state diffusion equation:

$$\begin{aligned} -\nabla \cdot (k(x)\nabla u(x)) &= f(x), \text{ in } \Omega \\ u(x) \Big|_{x \in \partial\Omega} &= 0 \end{aligned} . \quad (1)$$

Note that the equation (1) models not only diffusion, but also steady-state Darcy flow in porous media, steady-state heat conduction, etc. To address certain real-world problems, we use the Gaussian Random Field (GRF) to generate the field $\phi(x)$ with the following covariance models as functions of distance d :

- Cubic:

$$\text{Cov}(d) = \begin{cases} \sigma^2 \left(1 - 7\left(\frac{d}{l}\right)^2 + \frac{35}{4}\left(\frac{d}{l}\right)^3 - \frac{7}{2}\left(\frac{d}{l}\right)^5 + \frac{3}{4}\left(\frac{d}{l}\right)^7 \right), & d < l \\ 0, & d \geq l \end{cases} . \quad (2)$$

- Exponential:

$$\text{Cov}(d) = \sigma^2 \exp\left(-\frac{d}{l}\right) . \quad (3)$$

- Gaussian:

$$\text{Cov}(d) = \sigma^2 \exp\left(-\frac{d^2}{l^2}\right) . \quad (4)$$

The correlation length in each dataset is $l = 0.05$ and the complexity of a resulting dataset is controlled by variance σ^2 . The forcing term $f(x)$ is sampled from the standard normal distribution for each sampled PDE in each dataset. The resulting coefficient $k(x)$ is obtained with:

$$k(x) = \exp(\phi(x)) . \quad (5)$$

We propose to measure the complexity of the generated GRF with the global contrast in the field $\phi(x)$:

$$\text{contrast} = \exp\left(\max(\phi(x)) - \min(\phi(x))\right) . \quad (6)$$

Complexity grows with variance By increasing the variance σ^2 one can obtain a higher contrast (6) and thus a higher complexity of the PDE. This is a well-known phenomenon in applied numerical analysis and can be easily observed empirically. We illustrate this behaviour with the condition number $\kappa(A)$ of the matrices A obtained with discretization of the equation (1).

In the Table 1 one can observe that increasing σ^2 leads to a higher condition number $\kappa(A) = |\lambda_{\max}|/|\lambda_{\min}|$ of the discretized differential operator Capizzano [2003]. The condition number is closely related to the performance of the numerical methods used to solve PDEs Benzi et al. [2005], Elman et al. [2014]. A high condition number indicates that small changes in the input can lead to large changes in the output, making the problem ill-conditioned. This is particularly important in PDEs, where small perturbations can significantly affect the solution. Also, if iterative methods are used to solve the discretized PDE, a larger condition number means a larger number of iterations for unpreconditioned and most of preconditioned iterative methods Saad [2003].

Connection to real-world problems All of the above reasoning is done with regard to the frequent occurrence of such tasks in real world Hashmi [2014], Massimo [2013], Carr and Turner [2016], Oristaglio and Hohmann [1984], Muravleva et al. [2021], including composite materials modeling, heat transfer, geophysical problems, fluid flow modeling. In Figure 2 one can see a cross section of the x -permeability field along the z axis over the SPE10 model 2 benchmark Christie and Blunt [2001]. The term permeability is used to denote the coefficients of the above equation when considering flow in porous media. This field is very similar to the ConDiff samples in Figure 1.

This benchmark is well known in the field of reservoir modelling and fluid flow in porous media. SPE10 model 2 poses a significant challenge for the tasks of uncertainty quantification, upscaling and multiphase fluid flow modelling.

Table 1: Summary of the ConDiff with min, mean and max values of the contrast (6). ¹Condition number $\kappa(A)$ is calculated for a single sampled discretized (1).

Covariance	Variance	Min contrast	Mean contrast	Max contrast	$\kappa^1(A)$
Grid 64×64					
Cubic	0.1	$7.0 \cdot 10^0$	$1.0 \cdot 10^1$	$1.5 \cdot 10^1$	$3.6 \cdot 10^3$
	0.4	$5.0 \cdot 10^1$	$9.6 \cdot 10^1$	$2.5 \cdot 10^2$	$7.3 \cdot 10^3$
	1.0	$6.0 \cdot 10^2$	$8.3 \cdot 10^2$	$1.0 \cdot 10^3$	$2.0 \cdot 10^4$
	2.0	$8.0 \cdot 10^4$	$8.9 \cdot 10^4$	$1.0 \cdot 10^5$	$1.8 \cdot 10^5$
Exp	0.1	$6.0 \cdot 10^0$	$9.0 \cdot 10^0$	$1.5 \cdot 10^1$	$4.3 \cdot 10^3$
	0.4	$5.0 \cdot 10^1$	$8.5 \cdot 10^1$	$2.3 \cdot 10^2$	$5.2 \cdot 10^3$
	1.0	$6.0 \cdot 10^2$	$7.9 \cdot 10^2$	$1.0 \cdot 10^3$	$1.7 \cdot 10^4$
	2.0	$8.0 \cdot 10^4$	$8.9 \cdot 10^4$	$1.0 \cdot 10^5$	$1.9 \cdot 10^5$
Gauss	0.1	$5.0 \cdot 10^0$	$8.0 \cdot 10^0$	$1.4 \cdot 10^1$	$4.1 \cdot 10^3$
	0.4	$5.0 \cdot 10^1$	$7.5 \cdot 10^1$	$2.3 \cdot 10^2$	$8.1 \cdot 10^3$
	1.0	$6.0 \cdot 10^2$	$7.7 \cdot 10^2$	$1.0 \cdot 10^3$	$2.4 \cdot 10^4$
	2.0	$8.0 \cdot 10^4$	$8.9 \cdot 10^4$	$1.0 \cdot 10^5$	$8.8 \cdot 10^5$
Grid 128×128					
Cubic	0.1	$8.0 \cdot 10^0$	$1.1 \cdot 10^1$	$1.5 \cdot 10^1$	$1.6 \cdot 10^4$
	0.4	$5.5 \cdot 10^1$	$1.3 \cdot 10^2$	$2.5 \cdot 10^2$	$3.8 \cdot 10^4$
	1.0	$6.0 \cdot 10^2$	$8.8 \cdot 10^2$	$1.0 \cdot 10^3$	$1.0 \cdot 10^5$
	2.0	$8.0 \cdot 10^4$	$8.9 \cdot 10^4$	$1.0 \cdot 10^5$	$1.2 \cdot 10^6$
Exp	0.1	$6.0 \cdot 10^0$	$1.0 \cdot 10^1$	$1.5 \cdot 10^1$	$1.7 \cdot 10^4$
	0.4	$5.1 \cdot 10^1$	$1.1 \cdot 10^2$	$2.5 \cdot 10^2$	$3.3 \cdot 10^4$
	1.0	$6.0 \cdot 10^2$	$8.3 \cdot 10^2$	$1.0 \cdot 10^3$	$9.7 \cdot 10^4$
	2.0	$8.0 \cdot 10^4$	$8.9 \cdot 10^4$	$1.0 \cdot 10^5$	$6.3 \cdot 10^5$
Gauss	0.1	$5.0 \cdot 10^0$	$8.0 \cdot 10^0$	$1.4 \cdot 10^1$	$1.8 \cdot 10^4$
	0.4	$5.0 \cdot 10^1$	$7.8 \cdot 10^1$	$2.5 \cdot 10^2$	$7.2 \cdot 10^4$
	1.0	$6.0 \cdot 10^2$	$7.7 \cdot 10^2$	$1.0 \cdot 10^3$	$1.6 \cdot 10^5$
	2.0	$8.0 \cdot 10^4$	$8.9 \cdot 10^4$	$1.0 \cdot 10^5$	$1.5 \cdot 10^6$

Dataset description To generate the fields $\phi(x)$ we use the highly efficient `parafIELDS` library¹ with C++ backend. We use covariance models from {cubic, exponential, Gaussian} with 4 variance values from {0.1, 0.4, 1.0, 2.0}. We use the forcing term $f(x) \sim \mathcal{N}(0, 1)$. A Dirichlet boundary condition is set for each coefficient realization since boundary conditions do not contribute significantly to the resulting complexity Capizzano [2003]. The ground truth solution is obtained using cell-centered second-order finite volume method. The coefficients are in the center of cells, the values are in the nodes.

For each parameter set, we generate 1000 training and 200 test realizations of the diffusion equation (1) on 64×64 and 128×128 grids. Note that datasets with the same field parameters but different

¹<https://github.com/parafIELDS/parafIELDS>

grid sizes are generated independently and do not represent the same field. The fixed geometry of ConDiff allows PDEs with different fields $\phi(x)$ to be compared without fear that different geometries will interfere with a fair comparison across different coefficient functions. To control the complexity of the generated PDEs realizations, we set contrast bounds during generation as follows:

- $\sigma^2 = 0.1$, contrast $\in [5, 15]$,
- $\sigma^2 = 0.4$, contrast $\in [50, 250]$,
- $\sigma^2 = 1.0$, contrast $\in [6 \cdot 10^2, 10^3]$,
- $\sigma^2 = 2.0$, contrast $\in [8 \cdot 10^4, 10^5]$.

In total, ConDiff consists of 24 PDEs with different GRFs and grid sizes. Table 1 summarizes the properties of ConDiff. Figure 3 illustrates the contrast distributions. Coming back to the permeability cross section of SPE10 model 2 (Figure 2), it has contrast $= 2.5 \cdot 10^6$ according to (6). We want to emphasize that although the most complex coefficient of ConDiff is smaller by an order of magnitude compared to the cross section of SPE10 model 2, our experiments show that this coefficient is too complex for the chosen models to predict well.

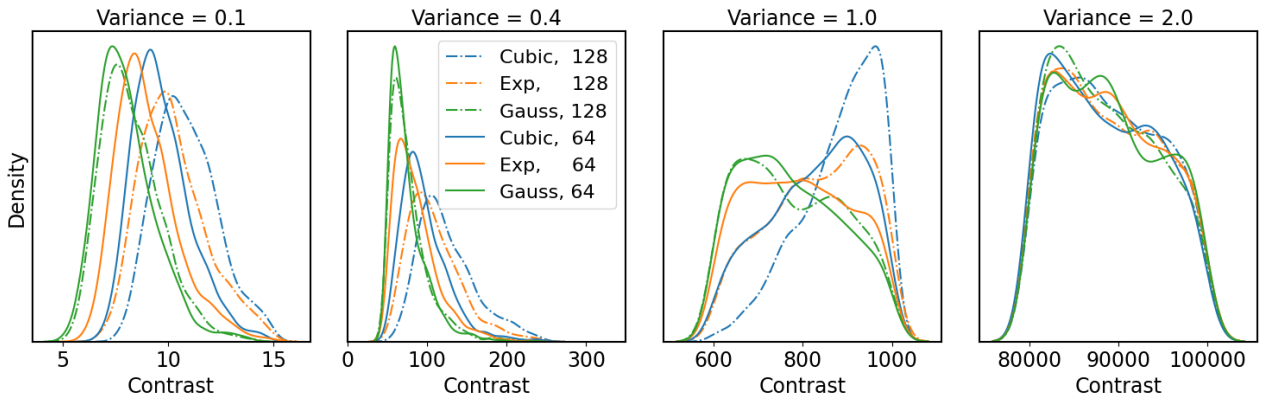


Figure 3: GRF contrast distribution for PDEs from Table 1.

3 Experiments

Models We do not attempt to benchmark every scientific machine learning surrogate model on the ConDiff. We have selected the following list of models to validate on the ConDiff: Spectral Neural Operator (SNO) Fanaskov and Oseledets [2023], Factorized Fourier Neural Operator (F-FNO) Tran et al. [2021], Dilated ResNet (DilResNet) Yu et al. [2017] and U-Net Ronneberger et al. [2015]. Neural operators FNO and SNO are both types of neural networks designed to learn mappings between function spaces, in particular to solve PDEs. Neural operators are designed to be universal approximators of continuous operators acting between Banach spaces and to be discretization invariant, meaning that they can handle different discretizations of the underlying function spaces without requiring changes to the model. DilResNet and U-Net are classical neural network models originating from the field of computer vision (CV). Both models have shown their applicability beyond CV and have been used extensively for modeling physical phenomena Stachenfeld et al. [2021], Ma et al. [2021]. More details about the models used can be found in the Appendix A.

Experiment environment For training neural networks we use frameworks from the JAX Bradbury et al. [2018] ecosystem: Equinox Kidger and Garcia [2021] and Optax DeepMind et al. [2020]. The loss function used is the relative L_2 loss:

$$L_2 = \frac{1}{N} \sum_{i=1}^N \frac{\|\hat{y}_i - y_i\|_2}{\|y_i\|_2} . \quad (7)$$

Training samples for the models are the values of the coefficient function $k(x)$ and the forcing term $f(x)$ in the grid cells. Targets are the values of the solution function $u(x)$ in the grid cells. We also use (7) as a primary performance metric, assessing the quality of the models' predictions, and report averaged values over the test set with standard deviation.

For all the problems we train for 400 epochs for grid = 64 and for 500 epochs for grid = 128. We use the AdamW optimizer with an initial learning rate equals to 10^{-3} and a weight decay equals to 10^{-2} . We use a learning rate schedule that halves the learning rate every 50 epochs. Each PDE realization has a dataset size of 1000 training samples and 200 test samples. We use a single GPU Nvidia Tesla V100 16Gb for training on grid = 64 and a single GPU Nvidia A40 48Gb for training on grid = 128.

Table 2: Results for Poisson equation.

Grid	SNO	F-FNO	DilResNet	U-Net
64	0.056 ± 0.018	0.027 ± 0.008	0.018 ± 0.005	0.020 ± 0.007
128	0.073 ± 0.021	0.047 ± 0.013	0.063 ± 0.016	0.267 ± 0.049

Table 3: Performance comparison of the models on the PDEs with the 64×64 grid from ConDiff.

Covariance	Variance	SNO	F-FNO	DilResNet	U-Net
Cubic	0.1	0.09 ± 0.02	0.07 ± 0.02	0.07 ± 0.02	0.08 ± 0.02
	0.4	0.15 ± 0.04	0.14 ± 0.03	0.14 ± 0.03	0.17 ± 0.04
	1.0	0.23 ± 0.06	0.22 ± 0.06	0.22 ± 0.06	0.24 ± 0.06
	2.0	0.35 ± 0.10	0.34 ± 0.09	0.35 ± 0.10	0.42 ± 0.10
Exp	0.1	0.12 ± 0.03	0.11 ± 0.03	0.11 ± 0.03	0.12 ± 0.04
	0.4	0.21 ± 0.06	0.21 ± 0.06	0.20 ± 0.06	0.26 ± 0.07
	1.0	0.33 ± 0.09	0.34 ± 0.09	0.36 ± 0.09	0.35 ± 0.09
	2.0	0.59 ± 0.14	0.58 ± 0.14	0.60 ± 0.13	0.64 ± 0.13
Gauss	0.1	0.12 ± 0.04	0.11 ± 0.04	0.11 ± 0.03	0.12 ± 0.03
	0.4	0.23 ± 0.06	0.22 ± 0.06	0.21 ± 0.06	0.25 ± 0.06
	1.0	0.38 ± 0.08	0.37 ± 0.09	0.38 ± 0.09	0.39 ± 0.09
	2.0	0.66 ± 0.14	0.65 ± 0.14	0.66 ± 0.13	0.72 ± 0.24

Table 4: Performance comparison of SNO and F-FNO on the PDEs with the 128×128 grid from ConDiff.

Covariance	Variance	SNO	F-FNO
Cubic	0.1	0.09 ± 0.03	0.08 ± 0.02
	0.4	0.15 ± 0.04	0.14 ± 0.04
	1.0	0.23 ± 0.06	0.22 ± 0.06
	2.0	0.36 ± 0.11	0.36 ± 0.10
Exp	0.1	0.13 ± 0.03	0.12 ± 0.03
	0.4	0.21 ± 0.07	0.21 ± 0.06
	1.0	0.33 ± 0.09	0.33 ± 0.08
	2.0	0.58 ± 0.15	0.57 ± 0.13
Gauss	0.1	0.13 ± 0.04	0.12 ± 0.03
	0.4	0.23 ± 0.06	0.23 ± 0.06
	1.0	0.37 ± 0.10	0.37 ± 0.10
	2.0	0.68 ± 0.13	0.66 ± 0.13

Validation on ConDiff We start the experiments with the Poisson equation and consider it as a special case of (1) with $k(x) = 1$ and contrast = 1. All models achieve an accuracy of the order of

10^{-2} (Table 2). Increasing the grid size leads to moderate increases in error, except for the U-Net for which the error increases by an order of magnitude.

The diffusion equation for grid 64 (Table 3) with covariances (2), (3) and (4) are more challenging for the models. While the performance on the diffusion equation with cubic covariance with $\sigma^2 = 0.1$ is comparable to the performance on the Poisson equation, the error on the diffusion equation with exponential and Gaussian covariances is already an order of magnitude higher. Increasing σ^2 leads to worse performance of each model on each PDE. The most complex PDE is the one generated with the Gaussian covariance model in GRF, which is also consistent with the condition number estimation in Table 1. Interestingly, the performance of FNO and SNO models on PDEs with grid 128 is not much different from PDEs on grid 64 (Table 4).

Table 5: Generalization of the models to unseen PDEs with different GRF covariance model with 64×64 grid and $\sigma^2 = 0.1$.

Train \ Test	SNO			F-FNO		
	Cubic	Exp	Gauss	Cubic	Exp	Gauss
Cubic	0.09 ± 0.02	0.12 ± 0.04	0.12 ± 0.03	0.07 ± 0.02	0.11 ± 0.03	0.11 ± 0.03
Exp	0.09 ± 0.03	0.12 ± 0.03	0.12 ± 0.04	0.08 ± 0.03	0.11 ± 0.03	0.11 ± 0.04
Gauss	0.09 ± 0.03	0.12 ± 0.03	0.12 ± 0.03	0.08 ± 0.02	0.11 ± 0.03	0.11 ± 0.04
DilResNet			U-Net			
Cubic	Cubic	Exp	Gauss	Cubic	Exp	Gauss
	0.07 ± 0.02	0.11 ± 0.04	0.11 ± 0.03	0.08 ± 0.02	0.12 ± 0.03	0.12 ± 0.03
Exp	0.07 ± 0.02	0.11 ± 0.03	0.11 ± 0.03	0.08 ± 0.03	0.11 ± 0.03	0.11 ± 0.04
Gauss	0.17 ± 0.06	0.25 ± 0.09	0.11 ± 0.04	0.08 ± 0.02	0.12 ± 0.04	0.12 ± 0.03

Table 6: Generalization of the models to unseen PDEs with different GRF covariance model with 64×64 grid and $\sigma^2 = 0.4$.

Train \ Test	SNO			F-FNO		
	Cubic	Exp	Gauss	Cubic	Exp	Gauss
Cubic	0.15 ± 0.04	0.22 ± 0.06	0.22 ± 0.07	0.14 ± 0.03	0.21 ± 0.06	0.21 ± 0.07
Exp	0.18 ± 0.05	0.21 ± 0.06	0.22 ± 0.06	0.15 ± 0.04	0.21 ± 0.06	0.22 ± 0.07
Gauss	0.17 ± 0.05	0.22 ± 0.06	0.23 ± 0.07	0.15 ± 0.04	0.21 ± 0.07	0.22 ± 0.06
DilResNet			U-Net			
Cubic	Cubic	Exp	Gauss	Cubic	Exp	Gauss
	0.14 ± 0.04	0.23 ± 0.07	0.23 ± 0.07	0.17 ± 0.06	0.24 ± 0.07	0.24 ± 0.07
Exp	0.14 ± 0.04	0.20 ± 0.06	0.22 ± 0.06	0.23 ± 0.08	0.26 ± 0.07	0.27 ± 0.08
Gauss	0.30 ± 0.10	0.24 ± 0.07	0.21 ± 0.06	0.21 ± 0.06	0.27 ± 0.08	0.26 ± 0.07

Transfer between parametric spaces Ideally, the surrogate model should handle transfers between different underlying parametric spaces of PDEs without loss of quality. In Tables 5, 6, 7, 8 show that in most experiments the error increases when training on cubic GRF and inferencing on exponential and Gaussian GRF. Conversely, the error decreases when training on Gaussian GRF and inferencing on cubic GRF.

Table 7: Generalization of the models to unseen PDEs with different GRF covariance model with 64×64 grid and $\sigma^2 = 1.0$.

Train \ Test	SNO			F-FNO		
	Cubic	Exp	Gauss	Cubic	Exp	Gauss
Cubic	0.23 ± 0.06	0.35 ± 0.09	0.39 ± 0.09	0.22 ± 0.06	0.34 ± 0.09	0.37 ± 0.09
Exp	0.25 ± 0.06	0.33 ± 0.09	0.38 ± 0.09	0.24 ± 0.06	0.34 ± 0.09	0.38 ± 0.09
Gauss	0.24 ± 0.07	0.35 ± 0.09	0.38 ± 0.08	0.24 ± 0.06	0.35 ± 0.09	0.37 ± 0.09
DilResNet			U-Net			
Cubic	Cubic	Exp	Gauss	Cubic	Exp	Gauss
	0.22 ± 0.06	0.35 ± 0.09	0.38 ± 0.09	0.24 ± 0.06	0.36 ± 0.09	0.38 ± 0.08
Exp	0.25 ± 0.07	0.36 ± 0.09	0.38 ± 0.10	0.25 ± 0.07	0.35 ± 0.09	0.38 ± 0.10
Gauss	0.57 ± 0.22	0.59 ± 0.22	0.38 ± 0.09	0.27 ± 0.07	0.36 ± 0.11	0.39 ± 0.09

Table 8: Generalization of the models to unseen PDEs with different GRF covariance model with 64×64 grid and $\sigma^2 = 2.0$.

Train \ Test	SNO			F-FNO		
	Cubic	Exp	Gauss	Cubic	Exp	Gauss
Cubic	0.35 ± 0.10	0.60 ± 0.14	0.70 ± 0.26	0.34 ± 0.09	0.61 ± 0.14	0.67 ± 0.19
Exp	0.39 ± 0.11	0.59 ± 0.14	0.69 ± 0.24	0.39 ± 0.11	0.58 ± 0.14	0.66 ± 0.15
Gauss	0.40 ± 0.11	0.60 ± 0.13	0.66 ± 0.14	0.37 ± 0.11	0.60 ± 0.13	0.65 ± 0.14
DilResNet			U-Net			
Cubic	Cubic	Exp	Gauss	Cubic	Exp	Gauss
	0.35 ± 0.10	0.61 ± 0.14	0.66 ± 0.15	0.42 ± 0.10	0.65 ± 0.14	0.68 ± 0.14
Exp	0.41 ± 0.10	0.60 ± 0.13	0.66 ± 0.17	0.53 ± 0.18	0.64 ± 0.13	0.72 ± 0.16
Gauss	0.72 ± 0.50	0.68 ± 0.20	0.66 ± 0.13	0.66 ± 0.40	0.69 ± 0.16	0.72 ± 0.24

4 Conclusion and Limitations

In summary, we propose a novel open-source dataset for the field of neural solving of PDEs. The unique feature of the dataset is discontinuous coefficients with high contrast for parametric PDEs from different distributions. By designing the coefficients in this way, we achieve a high complexity of the generated PDEs, which also illustrates real-world problems. The proposed complexity function allows to distinguish between the generated PDEs. We also provide code to generate new data based on the approach used in this paper. Furthermore, we validate a number of surrogate models on the ConDiff to illustrate its usefulness in the field of scientific machine learning.

It should be noted that the problems considered in this paper belong to the class of stochastic PDEs. The equation (1) has to be solved for a very large number of sampled coefficients when Monte Carlo or other methods are used to solve the stochastic PDEs. The surrogate models can help to significantly reduce the computational burden, so embedding the surrogate models tested on ConDiff into a Monte Carlo or similar stochastic PDEs solver is a reasonable next step.

Limitations of the proposed dataset are:

1. For practical numerical analysis, ConDiff is generated with small and moderate variances. The case of large variances has to be studied separately.
2. A linear elliptic parametric PDE is the basis of ConDiff, so other high contrast datasets are needed to test surrogate models for hyperbolic PDEs, nonlinear problems, etc.

3. ConDiff is generated on a regular rectangular grid. Other meshes and geometries may be required as an evolution of ConDiff. This may require more complex computational methods to obtain the ground truth solution.
4. Limited number of models validated on ConDiff. Comprehensive benchmark with different approaches (e.g. physics-informed neural networks, hybrid solvers) is needed.
5. The forcing term $f(x)$ is sampled from the standard normal distributions. While in this paper we focus on the complexity arising from discontinuous coefficients with high contrast, the right-hand side of a PDE can also significantly affect the complexity of the solving PDE. The case of complex forcing terms has to be studied separately.

References

George Em Karniadakis, Ioannis G Kevrekidis, Lu Lu, Paris Perdikaris, Sifan Wang, and Liu Yang. Physics-informed machine learning. *Nature Reviews Physics*, 3(6):422–440, 2021.

Zongyi Li, Nikola Kovachki, Kamyar Azizzadenesheli, Burigede Liu, Kaushik Bhattacharya, Andrew Stuart, and Anima Anandkumar. Fourier neural operator for parametric partial differential equations. *arXiv preprint arXiv:2010.08895*, 2020.

Rui Wang, Robin Walters, and Rose Yu. Incorporating symmetry into deep dynamics models for improved generalization. *arXiv preprint arXiv:2002.03061*, 2020.

Yohai Bar-Sinai, Stephan Hoyer, Jason Hickey, and Michael P Brenner. Learning data-driven discretizations for partial differential equations. *Proceedings of the National Academy of Sciences*, 116(31):15344–15349, 2019.

Randall J LeVeque. *Finite difference methods for ordinary and partial differential equations: steady-state and time-dependent problems*. SIAM, 2007.

Klaus-Jürgen Bathe. *Finite element procedures*. Klaus-Jurgen Bathe, 2006.

Robert Eymard, Thierry Gallouët, and Raphaèle Herbin. Finite volume methods. *Handbook of numerical analysis*, 7:713–1018, 2000.

Lloyd N Trefethen. *Spectral methods in MATLAB*. SIAM, 2000.

Shengze Cai, Zhiping Mao, Zhicheng Wang, Minglang Yin, and George Em Karniadakis. Physics-informed neural networks (pinns) for fluid mechanics: A review. *Acta Mechanica Sinica*, 37(12):1727–1738, 2021.

Hamidreza Eivazi, Yuning Wang, and Ricardo Vinuesa. Physics-informed deep-learning applications to experimental fluid mechanics. *Measurement science and technology*, 35(7):075303, 2024.

Maziar Raissi, Paris Perdikaris, and George E Karniadakis. Physics-informed neural networks: A deep learning framework for solving forward and inverse problems involving nonlinear partial differential equations. *Journal of Computational physics*, 378:686–707, 2019.

VS Fanaskov and Ivan V Oseledets. Spectral neural operators. In *Doklady Mathematics*, volume 108, pages S226–S232. Springer, 2023.

Lu Lu, Pengzhan Jin, Guofei Pang, Zhongqiang Zhang, and George Em Karniadakis. Learning nonlinear operators via deeponet based on the universal approximation theorem of operators. *Nature machine intelligence*, 3(3):218–229, 2021a.

Zongyi Li, Nikola Kovachki, Chris Choy, Boyi Li, Jean Kossaifi, Shourya Otta, Mohammad Amin Nabian, Maximilian Stadler, Christian Hundt, Kamyar Azizzadenesheli, et al. Geometry-informed neural operator for large-scale 3d pdes. *Advances in Neural Information Processing Systems*, 36, 2024.

Alasdair Tran, Alexander Mathews, Lexing Xie, and Cheng Soon Ong. Factorized fourier neural operators. *arXiv preprint arXiv:2111.13802*, 2021.

Steven L Brunton and J Nathan Kutz. *Data-driven science and engineering: Machine learning, dynamical systems, and control*. Cambridge University Press, 2022.

Patrick Schnell and Nils Thuerey. Stabilizing backpropagation through time to learn complex physics. *arXiv preprint arXiv:2405.02041*, 2024.

Jun-Ting Hsieh, Shengjia Zhao, Stephan Eismann, Lucia Mirabella, and Stefano Ermon. Learning neural pde solvers with convergence guarantees. *arXiv preprint arXiv:1906.01200*, 2019.

John Ingraham, Adam Riesselman, Chris Sander, and Debora Marks. Learning protein structure with a differentiable simulator. In *International conference on learning representations*, 2018.

Makoto Takamoto, Timothy Praditia, Raphael Leiteritz, Daniel MacKinlay, Francesco Alesiani, Dirk Pflüger, and Mathias Niepert. Pdebench: An extensive benchmark for scientific machine learning. *Advances in Neural Information Processing Systems*, 35:1596–1611, 2022.

Zhongkai Hao, Jiachen Yao, Chang Su, Hang Su, Ziao Wang, Fanzhi Lu, Zeyu Xia, Yichi Zhang, Songming Liu, Lu Lu, et al. Pinnacle: A comprehensive benchmark of physics-informed neural networks for solving pdes. *arXiv preprint arXiv:2306.08827*, 2023.

Yining Luo, Yingfa Chen, and Zhen Zhang. Cfdbench: A comprehensive benchmark for machine learning methods in fluid dynamics. *arXiv preprint arXiv:2310.05963*, 2023.

Pu Ren, N Benjamin Erichson, Shashank Subramanian, Omer San, Zarija Lukic, and Michael W Mahoney. Superbench: A super-resolution benchmark dataset for scientific machine learning. *arXiv preprint arXiv:2306.14070*, 2023.

Sungduk Yu, Walter Hannah, Liran Peng, Jerry Lin, Mohamed Aziz Bhouri, Ritwik Gupta, Björn Lütjens, Justus C Will, Gunnar Behrens, Julius Busecke, et al. Climsim: A large multi-scale dataset for hybrid physics-ml climate emulation. *Advances in Neural Information Processing Systems*, 36, 2024.

Andrzej Dulny, Andreas Hotho, and Anna Krause. Dynabench: A benchmark dataset for learning dynamical systems from low-resolution data. In *Joint European Conference on Machine Learning and Knowledge Discovery in Databases*, pages 438–455. Springer, 2023.

J Emmanuel Johnson, Quentin Febvre, Anastasiia Gorbunova, Sam Metref, Maxime Ballarotta, Julien Le Sommer, et al. Oceanbench: The sea surface height edition. *Advances in Neural Information Processing Systems*, 36, 2024.

Juan Nathaniel, Yongquan Qu, Tung Nguyen, Sungduk Yu, Julius Busecke, Aditya Grover, and Pierre Gentine. Chaosbench: A multi-channel, physics-based benchmark for subseasonal-to-seasonal climate prediction. *arXiv preprint arXiv:2402.00712*, 2024.

Artur Toshev, Gianluca Galletti, Fabian Fritz, Stefan Adami, and Nikolaus Adams. Lagrangebench: A lagrangian fluid mechanics benchmarking suite. *Advances in Neural Information Processing Systems*, 36, 2024.

Sheikh Md Shakeel Hassan, Arthur Feeney, Akash Dhruv, Jihoon Kim, Youngjoon Suh, Jaiyoung Ryu, Yoonjin Won, and Aparna Chandramowlishwaran. Bubbleml: A multi-physics dataset and benchmarks for machine learning. *arXiv preprint arXiv:2307.14623*, 2023.

Luke Bhan, Yuexin Bian, Miroslav Krstic, and Yuanyuan Shi. Pde control gym: A benchmark for data-driven boundary control of partial differential equations. *arXiv preprint arXiv:2405.11401*, 2024.

Jayesh K Gupta and Johannes Brandstetter. Towards multi-spatiotemporal-scale generalized pde modeling. *arXiv preprint arXiv:2209.15616*, 2022.

Yuanming Hu, Luke Anderson, Tzu-Mao Li, Qi Sun, Nathan Carr, Jonathan Ragan-Kelley, and Frédéric Durand. Difftaichi: Differentiable programming for physical simulation. *arXiv preprint arXiv:1910.00935*, 2019.

Lu Lu, Xuhui Meng, Zhiping Mao, and George Em Karniadakis. DeepXDE: A deep learning library for solving differential equations. *SIAM Review*, 63(1):208–228, 2021b. doi: 10.1137/19M1274067.

Philipp Holl, Vladlen Koltun, and Nils Thuerey. Learning to control pdes with differentiable physics. *arXiv preprint arXiv:2001.07457*, 2020.

Johannes Brandstetter, Daniel Worrall, and Max Welling. Message passing neural pde solvers. *arXiv preprint arXiv:2202.03376*, 2022.

Duc Minh Nguyen, Minh Chau Vu, Tuan Anh Nguyen, Tri Huynh, Nguyen Tri Nguyen, and Truong Son Hy. Neural multigrid memory for computational fluid dynamics. *arXiv preprint arXiv:2306.12545*, 2023.

Winfried Ripken, Lisa Coiffard, Felix Pieper, and Sebastian Dziadzio. Multiscale neural operators for solving time-independent pdes. *arXiv preprint arXiv:2311.05964*, 2023.

Andrey Bryutkin, Jiahao Huang, Zhongying Deng, Guang Yang, Carola-Bibiane Schönlieb, and Angelica Aviles-Rivero. Hamlet: Graph transformer neural operator for partial differential equations. *arXiv preprint arXiv:2402.03541*, 2024.

S Serra Capizzano. Generalized locally toeplitz sequences: spectral analysis and applications to discretized partial differential equations. *Linear Algebra and its Applications*, 366:371–402, 2003.

Michele Benzi, Gene H Golub, and Jörg Liesen. Numerical solution of saddle point problems. *Acta numerica*, 14:1–137, 2005.

Howard C Elman, David J Silvester, and Andrew J Wathen. *Finite elements and fast iterative solvers: with applications in incompressible fluid dynamics*. Oxford university press, 2014.

Yousef Saad. *Iterative methods for sparse linear systems*. SIAM, 2003.

M Saleem J Hashmi. *Comprehensive materials processing*. Newnes, 2014.

Luigi Massimo. *Physics of high-temperature reactors*. Elsevier, 2013.

EJ Carr and IW Turner. A semi-analytical solution for multilayer diffusion in a composite medium consisting of a large number of layers. *Applied Mathematical Modelling*, 40(15-16):7034–7050, 2016.

Michael L Oristaglio and Gerald W Hohmann. Diffusion of electromagnetic fields into a two-dimensional earth: A finite-difference approach. *Geophysics*, 49(7):870–894, 1984.

Ekaterina A Muravleva, Dmitry Yu Derbyshev, Sergei A Boronin, and Andrei A Osipov. Multigrid pressure solver for 2d displacement problems in drilling, cementing, fracturing and eor. *Journal of Petroleum Science and Engineering*, 196:107918, 2021.

Michael Andrew Christie and Martin J Blunt. Tenth spe comparative solution project: A comparison of upscaling techniques. *SPE Reservoir Evaluation & Engineering*, 4(04):308–317, 2001.

Fisher Yu, Vladlen Koltun, and Thomas Funkhouser. Dilated residual networks. In *Proceedings of the IEEE conference on computer vision and pattern recognition*, pages 472–480, 2017.

Olaf Ronneberger, Philipp Fischer, and Thomas Brox. U-net: Convolutional networks for biomedical image segmentation. In *Medical image computing and computer-assisted intervention—MICCAI 2015: 18th international conference, Munich, Germany, October 5-9, 2015, proceedings, part III* 18, pages 234–241. Springer, 2015.

Kimberly Stachenfeld, Drummond B Fielding, Dmitrii Kochkov, Miles Cranmer, Tobias Pfaff, Jonathan Godwin, Can Cui, Shirley Ho, Peter Battaglia, and Alvaro Sanchez-Gonzalez. Learned coarse models for efficient turbulence simulation. *arXiv preprint arXiv:2112.15275*, 2021.

Hao Ma, Yuxuan Zhang, Nils Thuerey, Xiangyu Hu, and Oskar J Haidn. Physics-driven learning of the steady navier-stokes equations using deep convolutional neural networks. *arXiv preprint arXiv:2106.09301*, 2021.

James Bradbury, Roy Frostig, Peter Hawkins, Matthew James Johnson, Chris Leary, Dougal Maclaurin, George Necula, Adam Paszke, Jake VanderPlas, Skye Wanderman-Milne, and Qiao Zhang. JAX: composable transformations of Python+NumPy programs, 2018. URL <http://github.com/google/jax>.

Patrick Kidger and Cristian Garcia. Equinox: neural networks in JAX via callable PyTrees and filtered transformations. *Differentiable Programming workshop at Neural Information Processing Systems 2021*, 2021.

DeepMind, Igor Babuschkin, Kate Baumli, Alison Bell, Surya Bhupatiraju, Jake Bruce, Peter Buchlovsky, David Budden, Trevor Cai, Aidan Clark, Ivo Danihelka, Antoine Dedieu, Claudio Fantacci, Jonathan Godwin, Chris Jones, Ross Hemsley, Tom Hennigan, Matteo Hessel, Shaobo Hou, Steven Kapturowski, Thomas Keck, Iurii Kemaev, Michael King, Markus Kunesch, Lena Martens, Hamza Merzic, Vladimir Mikulik, Tamara Norman, George Papamakarios, John Quan, Roman Ring, Francisco Ruiz, Alvaro Sanchez, Laurent Sartran, Rosalia Schneider, Eren Sezener, Stephen Spencer, Srivatsan Srinivasan, Miloš Stanojević, Wojciech Stokowiec, Luyu Wang, Guangyao Zhou, and Fabio Viola. The DeepMind JAX Ecosystem, 2020. URL <http://github.com/google-deepmind>.

A Architectures

In this section, we discuss the architectures used in more detail and provide information on the training procedures and hyperparameters used. The list of used models is:

1. F-FNO – Factorized Fourier Neural Operator (F-FNO) from Tran et al. [2021].
2. fSNO – Spectral Neural Operator (SNO). The construction mirrors FNO, but instead of FFT, a transformation based on Gauss quadratures is used Fanaskov and Oseledets [2023].
3. DilResNet – Dilated Residual Network from Yu et al. [2017], Stachenfeld et al. [2021].
4. U-Net – classical computer vision architecture introduced in Ronneberger et al. [2015].

A.1 F-FNO

Unlike the original Li et al. [2020], the authors of Tran et al. [2021] proposed to changing the operator layer to:

$$z^{\ell+1} = z^\ell + \sigma \left[W_2^{(\ell)} \sigma \left(W_1^{(\ell)} \mathcal{K}^{(\ell)}(z^{(\ell)}) + b_1^{(\ell)} \right) + b_2^{(\ell)} \right],$$

where σ is an activation function, W_1 and W_2 are weight matrices in the physical space, b_1 and b_2 are bias vectors and

$$\mathcal{K}^{(\ell)}(z^{(\ell)}) = \sum_{d \in D} \left[\text{IFFT}(R_d^{(\ell)} \cdot \text{FFT}_d(z^\ell)) \right],$$

where R_d is a Fourier domain weight matrix, FFT and IFFT are Fast Fourier and inverse Fast Fourier transforms.

F-FNO has an encoder-processor-decoder architecture. We used the following parameters: 4 Fourier layers in the processor, 12 modes and GeLU as the activation function. We used 48 features in the processor.

A.2 SNO

We utilized spectral neural operators (SNO) Fanaskov and Oseledets [2023] with linear integral kernels:

$$u \leftarrow \int dx A_{ij} p_j(x) (p_i, u) ,$$

where $p_j(x)$ are orthogonal or trigonometric polynomials.

These linear integral kernels are an extension of the integral kernels used in the FNO Li et al. [2020]. More specifically, starting from the input function u^n , we produce the output function u^{n+1} , which is later transformed by nonlinear activation. The transformation depends on the set of polynomials p_j that form a suitable basis for the problem at hand (e.g. trigonometric polynomials, Chebyshev polynomials, etc.). These polynomials are chosen beforehand and do not change during training. The transformation is naturally divided into three parts: analysis, processing, synthesis.

At the analysis stage, we find a discrete representation of the input function by projecting it onto a set of polynomials. To do this, we compute scalar products:

$$\alpha_j = (p_j, u^n) = \int dx p_j(x) u^n(x) w(x) ,$$

where $w(x)$ is a non-negative weight function given by the polynomial used.

At the processing stage, we process the obtained coefficients with a linear layer:

$$\alpha_i^* = \sum_j A_{ij} \alpha_j^*.$$

Finally, at the synthesis stage, we recover the continuous function as the sum of the processed coefficients:

$$u^{n+1} = \sum_j p_j \alpha_j^*.$$

We use SNO in Fourier basis (see Fanaskov and Oseledets [2023]) with encoder-processor-decoder architecture. The number of SNO layers is 4 and the number of $p_j(x)$ is 20. We use GeLU as activation function.

A.3 DilResNet

The conventional dilated residual network was first proposed in Stachenfeld et al. [2021]. In this study, the DilResNet architecture is configured with four blocks, each consisting of a sequence of convolutions with steps of $[1, 2, 4, 8, 4, 2, 1]$ and a kernel size of 3. Skip connections are also applied after each block and the GeLU activation function is used.

A.4 U-Net

We adopt the traditional U-Net architecture proposed in Ronneberger et al. [2015]. This U-Net configuration is characterised by a series of levels, where each level has approximately half the resolution of the previous one, and the number of features is doubled. At each level, we apply a sequence of three convolutions, followed by max pooling, and then a transposed convolution for upsampling. After upsampling, three more convolutions are applied at each level. The U-Net used in this study consists of four layers and incorporates the GeLU activation function.